RSC Advances

PAPER

View Article Online
View Journal | View Issue

Cite this: *RSC Adv.*, 2025, **15**, 38069

Multifunctional carbon-modified MoS_2 with expanded interlayer spacing and multiple exposed sulfur active sites for high-capacity Hg(II) adsorption

Mingmin Bai, *[a] Wenyuan Guo,[a] Yiyang Zhang,[a] Ruiqiang Yang[a] and Weixin Li*[b]

Received 28th June 2025
Accepted 29th September 2025

DOI: 10.1039/d5ra04594k

rsc.li/rsc-advances

A novel multifunctional carbon-modified MoS_2 material (C-W-D-MoS_2-*x*) was synthesized through a solvothermal method, exhibiting expanded interlayer spacing, a large surface area (~47.03 $m^2\ g^{-1}$), and abundant exposed sulfur (S) active sites that enabled efficient adsorption of Hg^{2+} from wastewater. Among the prepared variants, C-W-D-MoS_2-0.03 showed the highest adsorption performance, achieving an exceptional distribution coefficient (K_d) of 2.0 × 10^5 mL g^{-1}. The adsorption kinetics were best described by the pseudo-second-order model, while the adsorption isotherms were well-fitted to the Langmuir model, with a maximum adsorption capacity (q_m) of 1974.0 mg g^{-1}. This remarkable adsorption capability of C-W-D-MoS_2-0.03 can be attributed to the synergistic effect of carbon functional groups and the high density of S active sites. Furthermore, an alumina inorganic membrane functionalized with C-W-D-MoS_2-0.03 was successfully assembled into a device, demonstrating a dynamic removal process that reduced 50 mg L^{-1} of Hg^{2+} to below 0.1 mg L^{-1}.

1 Introduction

The contamination of water sources by mercury ions (Hg^{2+}) has attracted worldwide attention.[1,2] Hg^{2+} poses serious health risks by damaging the liver, brain, kidney, immune system, and nervous system due to its strong affinity for the enzymes and proteins containing sulfhydryl groups. More seriously, the human body cannot excrete Hg^{2+}, leading to its accumulation in biological organisms, which causes irreversible damage.[3–5] Consequently, the removal of Hg^{2+} from water has become an important concern.

Among the various technologies developed for mercury removal from wastewater, adsorption has emerged as one of the most effective strategies due to its simplicity, recyclability, low production cost, and commercial feasibility.[6–9] Conventional adsorbents such as graphene,[10] kaolin,[11] activated carbon,[12] metal–organic frameworks (MOFs),[13] and biomaterials[14] have been extensively studied. However, their performance is limited by the small number of physical adsorption sites with affinity for Hg^{2+}, resulting in low adsorption capacities and slow kinetics.[15,16] In recent years, guided by the theory of strong soft–soft interactions between mercury and sulfur, sulfide-containing compounds (S^{2-}) have emerged as highly effective adsorbents for mercury removal, including CdS,[17] CuS,[18] Co_3S_4,[19] and MoS_2.[20]

MoS_2 is composed of S-Mo-S layers, characterized by strong intralayer chemical bonds and weak van der Waals forces between adjacent layers. Owing to its high sulfur content, MoS_2 theoretically offers an adsorption capacity for Hg^{2+} of up to 2506 mg g^{-1}.[21,22] However, bulk MoS_2 demonstrates limited adsorption efficiency because its narrow interlayer spacing restricts Hg^{2+} ions from accessing the internal sulfur anions. Thus, increasing the number of exposed sulfur atoms is a key strategy to enhance the efficiency of Hg^{2+} removal from contaminated water. Expanding the interlayer spacing and introducing structural defects have proven effective for exposing more active sulfur atoms.[23–25] Previous studies have shown that when ammonium molybdate is employed as the raw material, the insertion of ammonium ions (NH_4^+) ions can widen the interlayer spacing of MoS_2.[26,27] Nonetheless, due to the relatively low concentration of NH_4^+ ions in such precursors, the widening effect remains limited. To address this, ammonia is used in the present work as the solvent, supplying a sufficient concentration of NH_4^+ ions to achieve more effective interlayer expansion.

Recently, coupling MoS_2 with carbon functional groups or biochar has also been regarded as a promising strategy for further enhancing its adsorption performance. The introduced carbon functional groups synergistically enhance the adsorption of Hg^{2+} in multiple ways. First, these groups provide additional adsorption sites that attract Hg^{2+} ions through

[a]School of Materials Science and Engineering, Jingdezhen Ceramic University, Jingdezhen 333403, PR China. E-mail: bellebai2010@126.com
[b]Department of Humanties, Jingdezhen University, Jingdezhen 333403, PR China. E-mail: weixin_li0708@163.com

Fig. 1 The process diagram of C-W-D-MoS_2-*x*.

electrostatic interactions. Second, certain functional groups, particularly –COOH, can act as Lewis bases and coordinate with the Lewis acidic Hg^{2+} to form stable surface complexes or π–π interactions.[21,28,29] Citric acid, a widely used organic acid, often serves as a complexing or capping agent capable of altering product morphology and introducing defects.[30,31] Under hydrothermal conditions, citric acid decomposes into carbon-containing byproducts (*i.e.*, carbon functional groups), which adsorb onto the surface of MoS_2 and further enhance its capacity to bind heavy metal ions.[30]

In this work, we aimed to design a carbon-modified MoS_2 with enlarged interlayer spacing and abundant exposed sulfur active sites for efficient Hg^{2+} adsorption. MoS_2 was synthesized *via* a simple one-step solvothermal process, where NH_4^+ ions in the mixed solvent served as intercalation agents to widen the interlayer spacing. Citric acid, used as a complexing agent, introduced structural defects, reduced particle size, and increased the specific surface area. Moreover, its decomposition during the hydrothermal reaction produced multifunctional carbon groups that anchored onto the MoS_2 surface. The combined effects of these modifications significantly enhanced the Hg^{2+} adsorption performance. Finally, MoS_2 was grown on an alumina inorganic membrane to evaluate its adsorption efficiency under dynamic flow conditions.

2 Materials and methods

2.1 Materials

Ammonium molybdate tetrahydrate ($(NH_4)_6Mo_7O_{24}\cdot 4H_2O$), thiourea ($CH_4N_2S$), hydrochloric acid (HCl), sodium hydroxide (NaOH), ethanol (C_2H_5OH), citric acid($C_6H_8O_7$), and ammonia solution ($NH_3\cdot H_2O$) were purchased from Aladdin Reagent Co., Ltd (China). All the reagents were of analytical grade and used without further purification.

2.2 Preparation of MoS_2

MoS_2 was synthesized *via* a one-step solvothermal method. Briefly, 0.002 mol of ammonium molybdate ($(NH_4)_6Mo_7O_{24}\cdot 4H_2O$), 0.035 mol of CH_4N_2S, and varying amounts of citric acid (0.01, 0.02, 0.03, and 0.04 mol) were dissolved in 40 mL of a mixed solvent consisting of 35 mL deionized water and 5 mL NH_4OH. The solution was magnetically stirred at room temperature (27 °C) at 200 rpm until fully homogeneous. After stirring for 30 min, the resulting precursor solution was transferred into a 100 mL hydrothermal reactor and heated at 200 °C for 24 h, followed by natural cooling to room temperature. The obtained products were washed three times with deionized water and C_2H_5OH by filtration, dried at 75 °C for 5 h, and denoted as C-W-D-MoS_2-*x* (carbon-modified, widened, defect-rich), where *x* represents the molar amount of citric acid. For comparison, traditional MoS_2 (T-MoS_2) was synthesized by dissolving 0.002 mol of $(NH_4)_6Mo_7O_{24}\cdot 4H_2O$ and 0.035 mol of CH_4N_2S in 40 mL of deionized water under the same reaction conditions described above. The schematic diagram of the synthesis process is shown in Fig. 1.

2.3 Preparation of alumina inorganic membrane functionalized with C-W-D-MoS_2-0.03

A single cleaned alumina inorganic membrane ($\varphi = 5 \times 1$, $L =$ 50 mm; Fig. S1) was immersed in the C-W-D-MoS_2-0.03 seed solution for 0.5 h. The membrane together with the solution was then placed in a hydrothermal reactor and reacted at 200 °C for 24 h. After the reaction, the membrane was removed, thoroughly washed with deionized water and C_2H_5OH, and dried at 75 °C for 10 h. The schematic illustration of the process is presented in Fig. 2.

2.4 Characterization

XRD analysis of the samples was carried out using a Rigaku D/max-(β) diffractometer with a scanning rate of 5° min^{-1}. The morphology of the samples was examined using SEM (JEOL JSM-6700F, Japan), TEM, and HRTEM (Titan G260-300). Raman spectra were recorded with a Raman spectrometer (HR800, Horiba Jobin Yvon). XPS spectra were obtained on a Thermo Scientific K-Alpha instrument equipped with an Al Kα X-ray source. The specific surface area and porosity were measured using nitrogen adsorption–desorption isotherms on a Micromeritics TriStar II 3020 analyzer. FT-IR spectra were collected using a Nicolet Nexus 470 FT-IR spectrometer. The

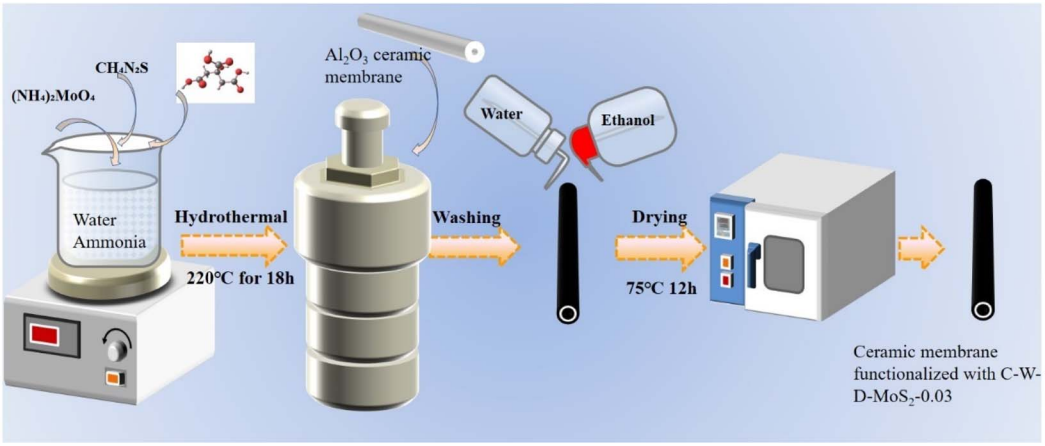

Fig. 2 The process diagram of alumina inorganic membrane functionalized with C-W-D-MoS_2-0.03.

concentration of Hg^{2+} ions in solution was determined by ICP-MS (iCAP Q, Thermo Fisher Scientific, USA).

2.5 Batch experiments of Hg^{2+} adsorption

The adsorption of Hg^{2+} was evaluated through batch experiments. A stock solution of $Hg(NO_3)_2$ (1000 mg L^{-1}) was diluted to the desired concentration, and the pH was adjusted using 1 M HNO_3 or 1 M NaOH. A measured amount of adsorbent was then added to the Hg^{2+} solution under controlled concentration and pH conditions. The suspension was magnetically stirred at 200 rpm at room temperature for a predetermined period. Subsequently, 3 mL of the solution was withdrawn, filtered through a 0.22 μm membrane, and analyzed for residual Hg^{2+} concentration. For adsorption kinetics, experiments were conducted in 50 mL of 200 mg L^{-1} Hg^{2+} solution using 20 mg of adsorbent over different contact times (0–180 min). The adsorption capacity of Hg^{2+} was calculated according to eqn (1):

$$q_e = \frac{(C_0 - C_e)V}{m} \quad (1)$$

where C_0 (mg L^{-1}) is the initial concentration of Hg^{2+}, C_e (mg L^{-1}) is the equilibrium concentration, V (L) is the volume of the solution, and m (g) is the mass of the adsorbent. The isotherm experiments were performed in 50 mL solutions with Hg^{2+} concentrations of 150, 200, 300, 400, and 500 mg L^{-1}, respectively.

2.6 Selectivity test experiments

Mixed solution consisting Hg^{2+}, Na^+, K^+, Pb^{2+}, Cu^{2+}, Mn^{2+} of 10 mg L^{-1} for each metal ion was used for investigating the relative selectivity of adsorbents at pH 5. Metal ions all came from their nitrates. After mixing an adsorbent with the solution for a certain period of time, 3 mL of the solution was filtered through a 0.22 μm membrane filter, and the concentration of metal ions were measured by ICP-MS.

2.7 Application device

Dynamic adsorption experiments were performed using a self-assembled test device consisting of a diaphragm pump and an alumina inorganic membrane functionalized with C-W-D-MoS_2-0.03, connected by flexible hoses. The diaphragm pump maintained a constant flow rate of 8 L min^{-1}, and the pure water flux of the functionalized membrane was measured as 10 m^3 (m^2 h). The filtrate was collected in a receiving tank and analyzed by ICP-MS. The device was continuously tested with 300 mL to 1 L of Hg^{2+}-contaminated wastewater (50 mg L^{-1}). To assess reusability, adsorption tests were carried out with 300 mL of wastewater at the same Hg^{2+} concentration (50 mg L^{-1}). For adsorption–desorption cycling, the functionalized alumina membrane was soaked and rinsed in 2 M HCl solution for 2 h, thoroughly washed with deionized water until neutral, and then dried at 70 °C for 12 h.

3 Results and discussion

3.1 Structure of MoS_2 materials

The morphology of MoS_2 plays a critical role in the adsorption process. As illustrated in Fig. 3 and S2, the SEM and TEM images reveal distinct morphological differences between T-MoS_2 and C-W-D-MoS_2-x (x = 0.01, 0.02, 0.03, and 0.04). In T-MoS_2 (Fig. 3(a) and (c)), the nanoflakes are stacked into flower-like structures, with each flake exhibiting an average thickness of ~5 nm and a lateral size of ~250 nm. By contrast, the morphology of C-W-D-MoS_2-x (Fig. 3(b), (d) and S2) evolves with increasing citric acid content, transitioning from flower-like assemblies to stacked structures and finally to fine nanoparticles. At x = 0.03, C-W-D-MoS_2-0.03 displays loosely aggregated microparticles with an average size of ~10 nm. This morphological transformation is mainly attributed to the chelating ability and steric hindrance of citric acid,[31] which increase porosity, expose more edge sites, and enhance the surface area of MoS_2. At higher citric acid concentrations, particularly in C-W-D-MoS_2-0.04, strong complexation results in densely stacked nanoparticles. The HRTEM images (Fig. 3(e) and (f)) further highlight these differences: T-MoS_2 exhibits a well-defined layered structure with an interlayer spacing of 6.5 Å, corresponding to the (002) plane,[24] whereas C-W-D-MoS_2-0.03 shows disordered or even missing layers in the yellow-circled regions due to the multifunctional carbon groups generated

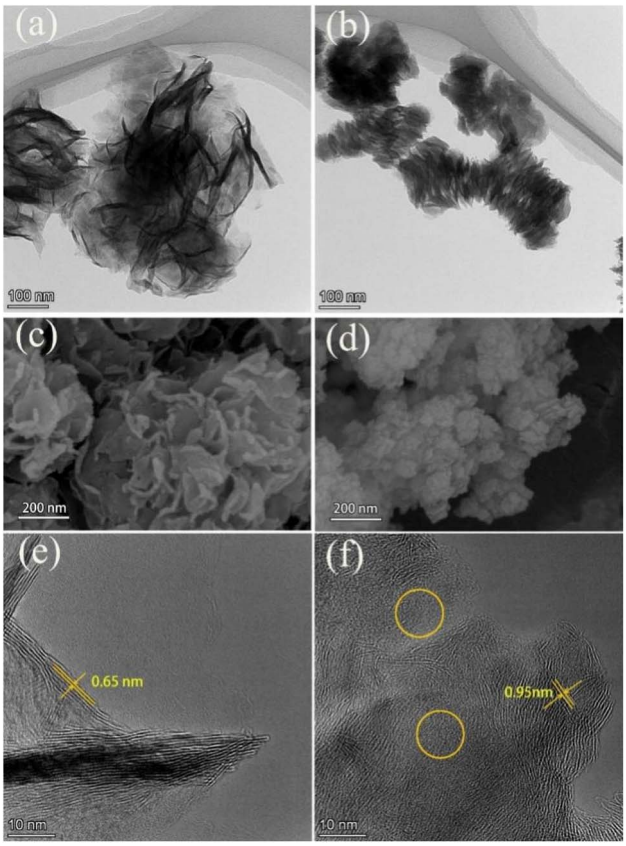

Fig. 3 TEM images of (a) T-MoS_2, (b) C-W-D-MoS_2-0.03, SEM images of (c) T-MoS_2, (d) C-W-D-MoS_2-0.03, HRTEM images of (e) T-MoS_2, (f) C-W-D-MoS_2-0.03.

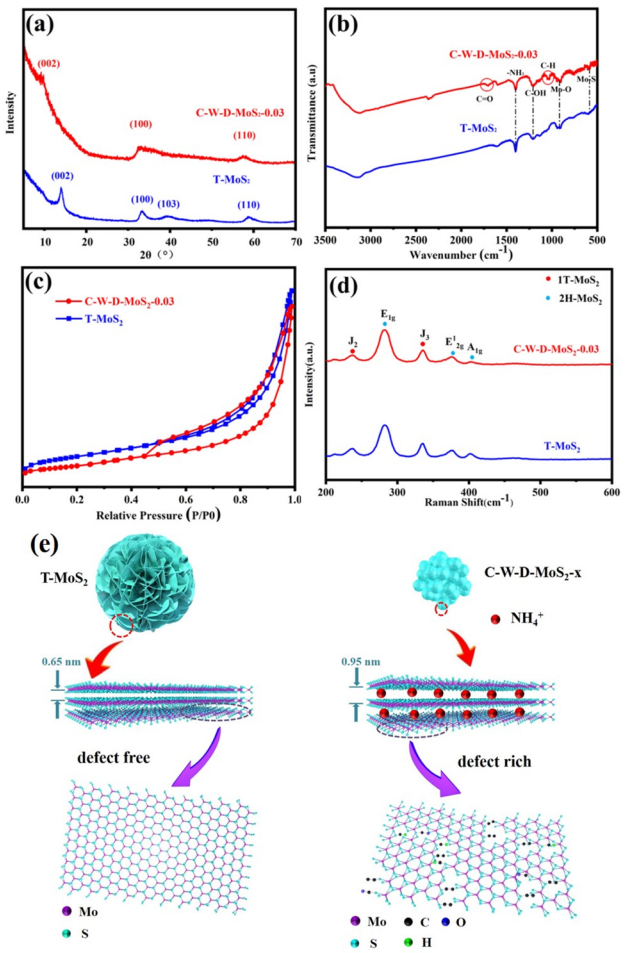

Fig. 4 XRD patterns (a), FT-IR spectra (b), N_2 adsorption–desorption isotherm (c), and Raman spectra (d) of T-MoS_2 and C-W-D-MoS_2-0.03, (e) structural diagrams of T-MoS_2 and C-W-D-MoS_2-x.

during the hydrothermal decomposition of citric acid. This disorder provides multiple exposed S active sites, thereby strengthening the interaction between sulfur and Hg^{2+}. Moreover, the intercalation of NH_4^+ ions (radius = 1.49 Å) expands the interlayer spacing of C-W-D-MoS_2 to 9.5 Å.[32,33]

Fig. 4(a) and S3(a) show the XRD patterns of T-MoS_2 and C-W-D-MoS_2-x. Four diffraction peaks at $2\theta = 14.3°$, 33.4°, 39.5°, and 58.8° correspond to the (002), (100), (103), and (110) planes of T-MoS_2, respectively.[6] For C-W-D-MoS_2-x, the characteristic (002) peak at 14.2° shifted to a lower angle of 9.2°, indicating an increase in interlayer spacing from 6.5 Å to 9.5 Å according to Bragg's law. This result is consistent with the interlayer distance observed in the HRTEM images and can be attributed to the intercalation of NH_4^+[32,33] and carbon functional groups.[36,37] In addition, the decreased intensity of diffraction peaks in C-W-D-MoS_2-x suggests that citric acid reduces crystallinity. These findings confirm that both the crystallinity and interlayer spacing of C-W-D-MoS_2-x can be intentionally regulated, thereby tuning the ratio of exposed unsaturated coordination sulfur sites. The FT-IR spectra of T-MoS_2 and C-W-D-MoS_2-x are shown in Fig. 4(b) and S3(b). The vibrational bands at 1403 cm^{-1}, 1207 cm^{-1}, 912 cm^{-1}, and 455 cm^{-1} correspond to –NH_3, C–OH, Mo–O, and Mo–S groups, respectively. Moreover, peaks at 1708 cm^{-1} and 1035 cm^{-1} in C-W-D-MoS_2-x are assigned to C=O and C–H stretching vibrations,[21,38] confirming the incorporation of carbon functional groups. The peak at 2353 cm^{-1} is attributed to CO_2 adsorbed on the sample surface.

Table 1 Detailed analysis results obtained from N_2 adsorption–desorption of T-MoS_2 and C-W-D-MoS_2-x

Samples	SSA_{BET} ($m^2\ g^{-1}$)	Pore volume ($cm^3\ g^{-1}$)	Pore size (nm)
T-MoS_2	5.67	0.027	19.72
C-W-D- MoS_2-0.01	13.81	0.086	13.35
C-W-D- MoS_2-0.02	5.52	0.043	19.72
C-W-D- MoS_2-0.03	30.21	0.103	9.55
C-W-D- MoS_2-0.04	13.05	0.078	12.87

The specific surface area and porosity directly influence adsorption efficiency. As shown in Fig. 4(c) and (d) and S3(c), the slit-shaped pores formed by stacked nanosheets give rise to type IV physisorption isotherms with H3 hysteresis loops in T-MoS_2 and C-W-D-MoS_2-x ($x = 0.01$, 0.02, 0.04). In contrast, C-W-D-MoS_2-0.03 exhibits an H4 hysteresis loop, suggesting the coexistence of both micropores and mesopores. The porosity and specific surface area of T-MoS_2 and C-W-D-MoS_2-x are

summarized in Table 1. As shown, T-MoS_2 exhibits a smaller specific surface area and pore volume, which can be attributed to the larger size of its individual MoS_2 nanosheets. Upon the introduction of citric acid, the nanosheet size decreases, leading to a significant increase in both specific surface area and pore volume. Notably, C-W-D-MoS_2-0.03 achieves the highest values, with a specific surface area of 30.21 $m^2 \cdot g^{-1}$ and a pore volume of 0.103 $cm^3 \cdot g^{-1}$. However, the finer stacking of nanosheets in this sample results in a slight reduction in pore size.

The Raman spectra of T-MoS_2 and C-W-D-MoS_2-x are shown in Fig. 4(d) and S3(d). For both T-MoS_2 and C-W-D-MoS_2-x, characteristic Raman peaks of the 2H phase (E_{1g}, $E_{2g}{}^1$, A_{1g}) and the 1T phase (J_2, J_3) are clearly observed.[39–41] These results are consistent with the XPS analysis, confirming the coexistence of both 1T and 2H phases in T-MoS_2 and C-W-D-MoS_2-x.[42,43] The corresponding structural diagrams are illustrated in Fig. 4(e). As shown, the intercalation of NH_4^+ ions leads to expansion of the MoS_2 interlayer spacing, while the strong chelating effect of citric acid alters the morphology of MoS_2 and introduces additional defects. At the same time, carbon functional groups generated from the hydrothermal decomposition of citric acid are adsorbed on both the inner and outer surfaces of MoS_2, thereby creating abundant adsorption sites.

XPS was employed to investigate the phase composition of the synthesized T-MoS_2 and C-W-D-MoS_2 materials. The full survey spectrum is presented in Fig. S5, while the high-resolution spectra of each element for T-MoS_2 and C-W-D-MoS_2-0.03 are shown in Fig. 5(a–f). In Fig. 5(a), the characteristic peaks of Mo $3d_{5/2}$ and Mo $3d_{3/2}$ for 1T-MoS_2 are observed at 227.89 eV and 231.13 eV, respectively, whereas the peak at 231.53 eV corresponds to Mo $3d_{3/2}$ in 2H-MoS_2.[34] Similarly, in Fig. 5(b), two peaks at 160.68 eV and 162.08 eV are attributed to S $2p_{3/2}$ and S $2p_{1/2}$ of the 1T phase, while the peak at 161.83 eV is assigned to S $2p_{1/2}$ of the 2H phase.[35] These results confirm the coexistence of both 1T and 2H phases in T-MoS_2.

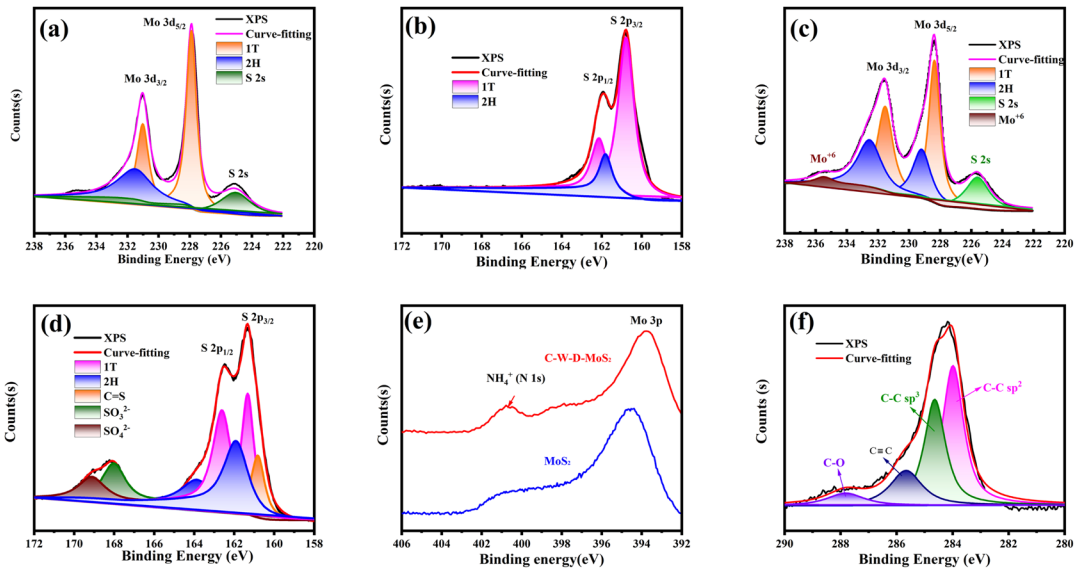

Fig. 5 High resolution XPS spectra and the fitting curves of T-MoS_2 and C-W-D-MoS_2-0.03 for Mo 3d (a and c), S 2p (b and d), N 1s (e) and C 1s (f).

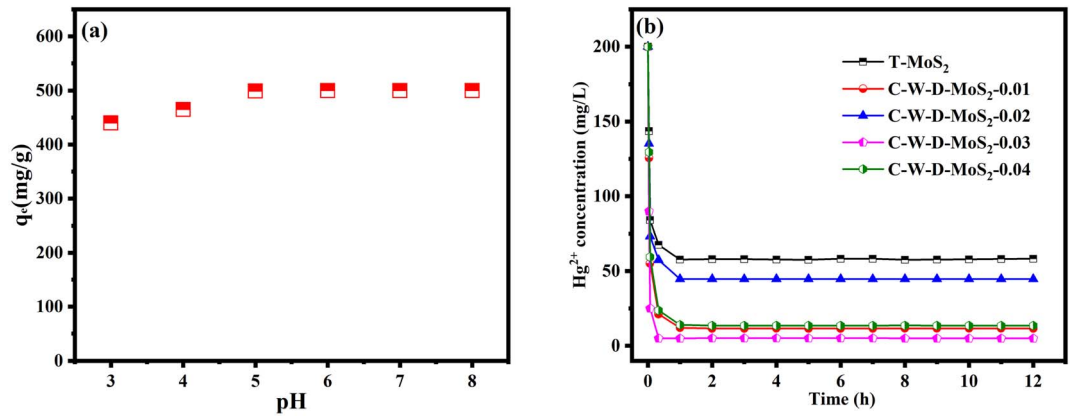

Fig. 6 (a) The influence of pH on the adsorption of Hg^{2+} by C-W-D-MoS_2-0.03, (b) Hg^{2+} adsorption curves of C-W-D-MoS_2-x adsorbents.

Table 2 Absorptivity of T-MoS_2 and C-W-D-MoS_2-x for Hg^{2+a}

Samples	C_e-12 h (mg L^{-1})	q_e-12 h (mg g^{-1})	Partition coefficient K_d (mL g^{-1})
T-MoS_2	57.63	711.85	0.12×10^5
C-W-D-MoS_2-0.01	11.54	942.30	0.81×10^5
C-W-D-MoS_2-0.02	44.67	776.65	0.17×10^5
C-W-D-MoS_2-0.03	4.91	975.5	2.0×10^5
C-W-D-MoS_2-0.04	13.46	932.70	0.69×10^5

[a] Experimental conditions: initial concentration Hg^{2+} 200 mg L^{-1} at pH = 5, 20 mg sorbent, 100 mL solution.

The fitting curves of Mo 3d for C-W-D-MoS_2-0.03 are presented in Fig. 5(c). Compared with T-MoS_2, additional peaks appear at 229.23 eV and 235.53 eV, corresponding to Mo $3d_{3/2}$ in 2H-MoS_2 and Mo^{6+} species, respectively. The calculated ratio of 1T to 2H phases is 2.1 for T-MoS_2, whereas it decreases to 1.1 in C-W-D-MoS_2-0.03. This result demonstrates that the introduction of citric acid reduces the proportion of the 1T phase in MoS_2. Since the 1T phase plays a critical role in adsorption due to its higher electrical conductivity and abundant unsaturated coordination sites,[6,26] regulating the 1T/2H phase ratio directly impacts the adsorption efficiency.

The S 2p spectrum of C-W-D-MoS_2-0.03 exhibits notable differences compared to that of T-MoS_2, as shown in Fig. 5(d). In particular, the peak at 160.78 eV is assigned to the C=S bond, confirming the interaction between carbon and sulfur. Additional peaks at 168.03 eV and 169.13 eV correspond to SO_3^{2-} and SO_4^{2-} species, respectively. The presence of Mo^{6+}, SO_3^{2-}, and SO_4^{2-} indicates partial surface oxidation of C-W-D-MoS_2-0.03 during the solvothermal process. The N 1s spectrum of C-W-D-MoS_2-0.03 (Fig. 5(e)) reveals a distinct peak associated with NH_4^+ ions, which is consistent with the interlayer expansion observed in TEM analysis.

The C 1s spectrum of C-W-D-MoS_2-0.03 (Fig. 5(f)) is deconvoluted into four peaks: 284.03 eV and 284.68 eV correspond to C–C (sp^2) and C–C (sp^3) bonding, respectively; while the peaks at 285.68 eV and 287.78 eV are attributed to C≡C and C–O groups.[21] These carbon functional groups originate from the decomposition of citric acid during hydrothermal synthesis, as well as subsequent oxidation of carbon species by O_2. The incorporation of these functional groups provides additional active sites, enhancing the adsorption affinity of C-W-D-MoS_2-0.03 toward Hg^{2+} ions.

3.2 Absorptivity of T-MoS_2 and C-W-D-MoS_2 for Hg(II)

The pH of the solution plays a crucial role in determining both the zeta potential of MoS_2 and the speciation of Hg(II). In this study, the solution pH was adjusted to a range of 3.0–8.0 using diluted NaOH and HNO_3. The zeta potential values of C-W-D-MoS_2-0.03 are presented in Table S1. The Zeta potential of C-W-D-MoS_2-0.03 remains negative across different pH values, indicating a negatively charged surface. A more negative surface charge enhances the electrostatic attraction between the adsorbent and Hg^{2+} ions, thereby promoting adsorption.[6,25] The adsorption experiments were conducted by adding 20 mg of the adsorbent to 50 mL of Hg^{2+} solution with an initial concentration of 200 mg L^{-1}. As illustrated in Fig. 6(a), the adsorption capacity of C-W-D-MoS_2-0.03 increases with rising pH, reaching its maximum at pH 5.0, after which it remains relatively stable. Considering the possible precipitation of Hg^{2+} due to its reaction with OH^- at higher pH values, the solution pH was maintained at 5.0 for subsequent experiments.[21,25]

The Hg^{2+} adsorption performance of various T-MoS_2 and C-W-D-MoS_2-x adsorbents was evaluated at room temperature. As illustrated in Fig. 6(b), the Hg^{2+} concentration decreases sharply in the initial stage, indicating rapid and effective adsorption. After 12 h, the removal efficiencies of T-MoS_2, C-W-D-MoS_2-0.01, C-W-D-MoS_2-0.02, C-W-D-MoS_2-0.03, and C-W-D-MoS_2-0.04 reached 70.89%, 94.23%, 77.67%, 97.55%, and 93.27%, respectively. Among these, C-W-D-MoS_2-0.03 demonstrated the most superior adsorption capacity. The corresponding adsorption parameters are summarized in Table 2. Notably, the maximum adsorption capacity (q_e) of C-W-D-MoS_2-0.03 is approximately 1.4 times higher than that of T-MoS_2. In contrast, the q_e value of C-W-D-MoS_2-0.02 is lower than those of C-W-D-MoS_2-0.01, C-W-D-MoS_2-0.03, and C-W-D-MoS_2-0.04, which may

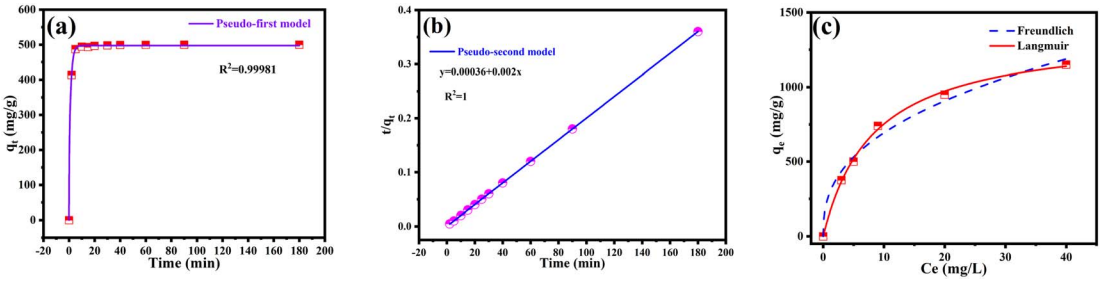

Fig. 7 Adsorption kinetics of C-W-D-MoS_2-0.03 (a) based on Pseudo first model, (b) based on Pseudo second model, (c) adsorption isotherm of C-W-D-MoS_2-0.03.

be attributed to the stacking of MoS_2 nanosheets. Furthermore, the distribution coefficient (K_d), calculated using eqn (2), reflects the adsorbent's affinity toward Hg^{2+}.

$$K_d = \frac{q_e}{C_e} \quad (2)$$

where C_e (mg L^{-1}) represents the equilibrium concentration and q_e (mg g^{-1}) denotes the amount adsorbed at C_e (mg L^{-1}).[44,45] As presented in Table 2, the K_d values of the C-W-D-MoS_2-x samples are consistently higher than that of T-MoS_2. Remarkably, the K_d value of C-W-D-MoS_2-0.03 is 16.5 times greater than that of T-MoS_2, highlighting its superior affinity and adsorption efficiency toward Hg^{2+}. Beyond the effect of the 1T phase on adsorption performance, factors such as specific surface area, porosity, and adsorption energy also play critical roles. Consequently, even though the 1T phase content in C-W-D-MoS_2 is reduced, its overall adsorption performance remains superior to that of T-MoS_2.

3.3 Adsorption behavior and mechanism of C-W-D-MoS_2-0.03

Adsorption kinetics and isotherms were investigated to clarify the adsorption mechanism of C-W-D-MoS_2-0.03. As illustrated in Fig. 7(a), the adsorption capacity of C-W-D-MoS_2-0.03 for Hg^{2+} increased rapidly during the first 5 minutes and gradually reached equilibrium within 20–30 minutes. The kinetic behavior was evaluated using both the pseudo-first-order and pseudo-second-order models, with the corresponding equations expressed as follows:[20,46]

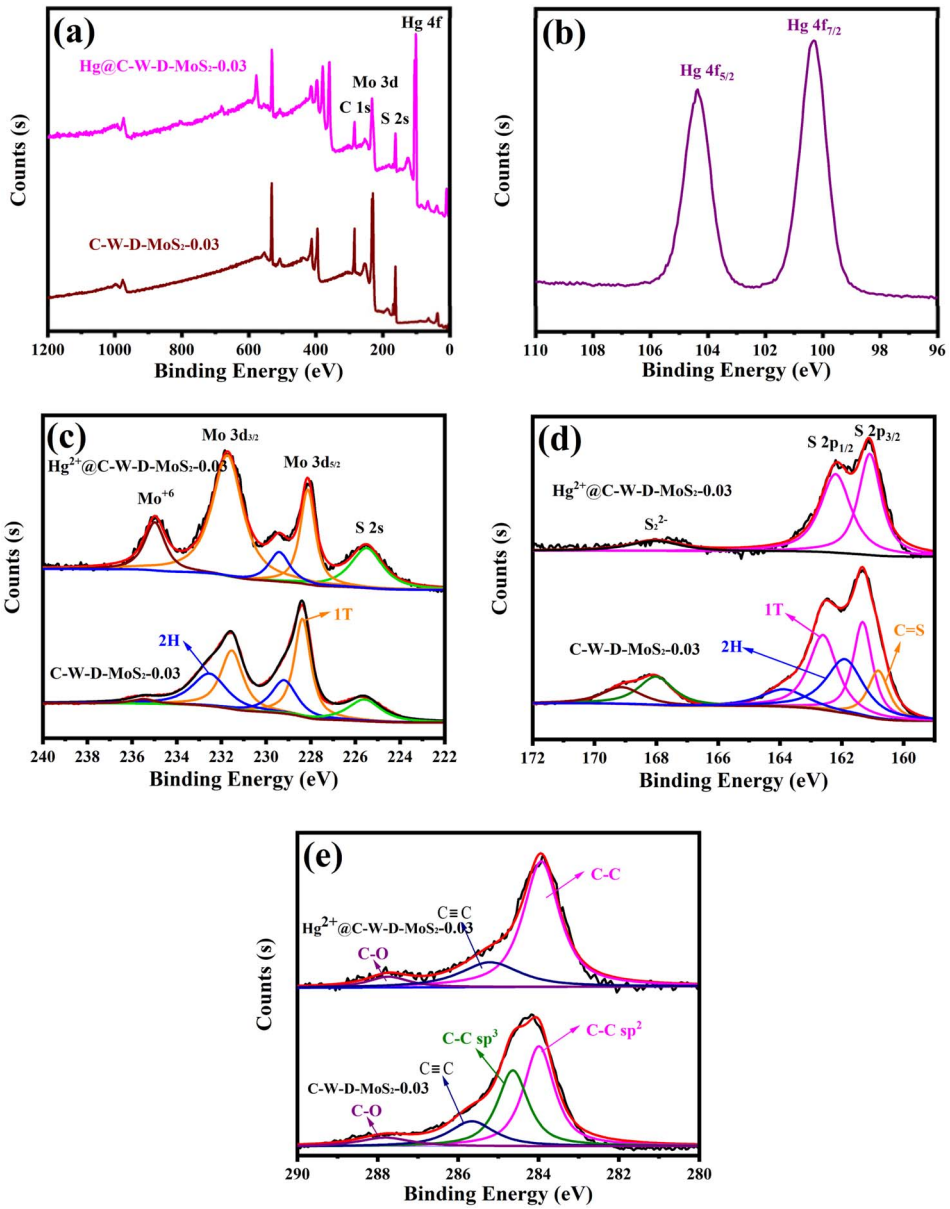

Fig. 8 XPS spectra of C-W-D-MoS_2-0.03 before and after adsorption. Full XPS spectra (a), XPS spectra of Hg 4f (b), Mo 3d (c), S 2p (d) and C 1s (e).

$$\ln(q_e - q_t) = \ln(q_e) - k_1 t \quad (3)$$

$$\frac{t}{q_t} = \frac{1}{k_2 q_e^2} + \frac{t}{q_e} \quad (4)$$

Here, q_e represents the equilibrium adsorption capacity, q_t denotes the adsorption capacity at time t (min), and k_1 (min^{-1}) and k_2 (g mg^{-1} min^{-1}) are the rate constants of the respective models. As shown in Fig. 7(a), the pseudo-first-order model demonstrates a strong correlation with an R^2 value of 0.999. However, the pseudo-second-order model, illustrated in Fig. 7(b), provides an even better fit with $R^2 = 1$, indicating that the adsorption kinetics of Hg^{2+} ions on C-W-D-MoS_2-0.03 are best described by the pseudo-second-order model. The rate constant k_2 was determined to be 0.11 g mg^{-1} min^{-1}. Compared with other MoS_2-based adsorbents,[21,25] C-W-D-MoS_2-0.03 exhibits a significantly faster adsorption rate, which can be attributed to its enlarged interlayer spacing, abundant sulfur sites, and the synergistic contribution of carbon-containing groups. The kinetic data and parameters for T-MoS_2 are provided in Fig. S6 and Table S2.

The adsorption isotherm of C-W-D-MoS_2-0.03, shown in Fig. 7(c), was employed to investigate its adsorption capacity for Hg^{2+}. As the concentration of Hg^{2+} increased, the equilibrium adsorption capacity correspondingly rose. The isotherm data were analyzed using both the Langmuir and Freundlich models:[47,48]

$$\text{Langmuir isotherm}: \frac{C_e}{q_e} = \frac{C_e}{q_m} + \frac{1}{q_m K_L} \quad (5)$$

$$\text{Freundlich isotherm}: \ln q_e = \ln K_F + b_F \ln C_e \quad (6)$$

Here, q_m (mg g^{-1}) denotes the maximum adsorption capacity of the adsorbent, while K_L (L mg^{-1}) and K_F represent the Langmuir and Freundlich adsorption constants, respectively, and b_F is a constant reflecting adsorption intensity. The fitted parameter values are summarized in Table S3. The adsorption isotherm of C-W-D-MoS_2-0.03 is better described by the Langmuir model, with an R^2 value of 0.996, compared to 0.985 for the Freundlich model. The Langmuir model suggests chemisorption behavior and monolayer adsorption, indicating strong adsorption capacity, particularly at low equilibrium concentrations. Based on the Langmuir isotherm model, the q_m value for Hg^{2+} adsorption on C-W-D-MoS_2-0.03 was calculated to be 1974.0 mg g^{-1}, confirming its high efficiency as an adsorbent for Hg^{2+}.[21,49] The adsorption isotherm of T-MoS_2 is shown in Fig. S7.

The adsorption mechanism of C-W-D-MoS_2-0.03 toward Hg^{2+} was further examined using XPS spectra obtained before and after adsorption.

From the full XPS spectra of C-W-D-MoS_2-0.03 after adsorption (Fig. 8(a)), distinct characteristic peaks of Hg^{2+} are clearly observed. The Hg 4f peaks at 100.35 eV and 104.35 eV (Fig. 8(b)) are close to those of Hg in HgS (100.7 eV, 104.8 eV),[38,50,51] confirming a chemical reaction between C-W-D-MoS_2-0.03 and Hg(II). The Mo XPS spectrum (Fig. 8(c)) shows an increase in the Mo^{6+} peak intensity after adsorption, suggesting partial oxidation of Mo during the process. Moreover, the peak area of Mo 3d in the 2H phase decreases, while that in the 1T phase increases. A similar pattern is observed in the S 2p XPS spectrum (Fig. 8(d)), where the 2H phase peak significantly diminishes and disappears following Hg(II) adsorption. The enhancement of the 1T phase is attributed to the strong interactions between adsorbed Hg ions and Mo and S ions, which stabilize the 1T phase in MoS_2.[52] Additionally, as shown in Fig. 8(e), the C–C sp^3 bonding peak vanishes, whereas the C–C sp^2 peak increases after Hg(II) adsorption. The disappearance of the sp^3 peak indicates that synergistic π–π interactions between carbon functional groups contribute to the efficient adsorption of Hg^{2+}.[53] These findings suggest that the carbon groups generated from citric acid hydrolysis play a pivotal role in enhancing the adsorption performance of C-W-D-MoS_2-0.03 through synergistic effects.

3.4 Sensitivity for Hg^{2+}

In actual industrial wastewater, there are generally competing metal ions coexisting with Hg^{2+}. Therefore, competitive adsorption tests were carried out to determine the specificity of C-W-D-MoS_2-0.03 toward Hg^{2+} ions. A variety of interfering cations were added to the experimental solution, including

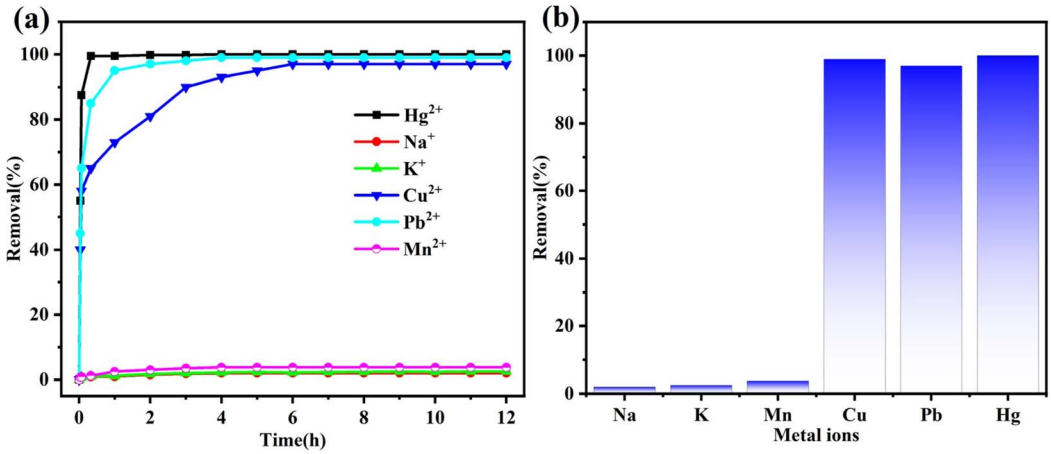

Fig. 9 (a) Time-dependent removal efficiency of various ions, (b) adsorption selectivity of C-W-D-MoS_2-0.03.

Table 3 The adsorption data of C-W-D-MoS_2-0.03 and other MoS_2-derived advanced sorbents for Hg(II)

Sorbent	M^{2+}	q_m (mg g^{-1})	Partition coefficient K_d	Ref.
Au/Fe_3O_4/MoS_2 CAs	Hg^{2+}	1527	1.82×10^8 mL g^{-1}	38
2D MoS_2	Hg^{2+}	584.8	6.24×10^3 mL g^{-1}	50
MoS_2/CNF_2	Hg^{2+}	553.8	—	27
d-MoS_2/Fe_3O_4	Hg^{2+}	425.5	2.97×10^7 mL g^{-1}	25
3D-MoS_2-rGO	Hg^{2+}	400.0	1.9×10^4 mL g^{-1}	51
3D-MoS_2	Hg^{2+}	1527.0	0.5×10^5 mL g^{-1}	49
C-MoS_2	Hg^{2+}	1957.0	0.45×10^5 mL g^{-1}	21
W-DR-N-MoS_2	Hg^{2+}	2563	3.53×10^8 mL g^{-1}	24
C-W-D-MoS_2-0.03	Hg^{2+}	1974.0	2×10^5 mL g^{-1}	This paper

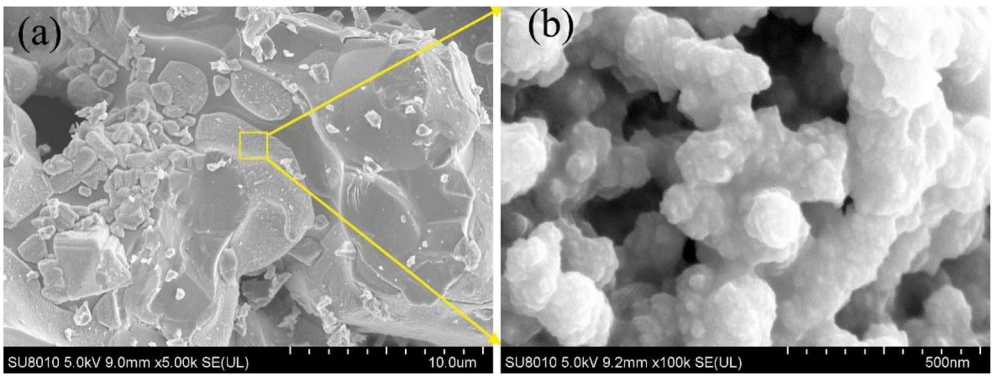

Fig. 10 (a) SEM image of alumina inorganic membrane functionalized with C-W-D-MoS_2-0.03, (b) enlarged image.

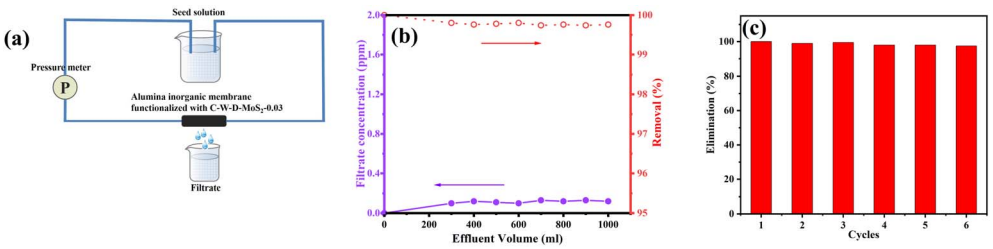

Fig. 11 (a) The diagram of test device in the laboratory, (b) the curves of adsorption efficiency, (c) the elimination of alumina inorganic membrane functionalized with C-W-D-MoS_2-0.03 during six cycles.

common heavy metal ions (Pb^{2+}, Cu^{2+}, Mn^{2+}) and alkali metal ions (K^+ and Na^+). From Fig. 9, the removal efficiency and adsorption kinetic of Hg^{2+} do not change in the presence of these competing ions, indicating that they do not interfere with the Hg^{2+}. The absorption efficiency for Hg^{2+} can reach 100% within 5 minutes, whereas the time to reach adsorption equilibrium of Pb^{2+}, Cu^{2+} are 4 h and 6 h, respectively. Hg^{2+} are preferentially adsorbed by C-W-D-MoS_2-0.03, that we may control the selectivity of these heavy metal ions (Pb^{2+}, Cu^{2+}) during Hg^{2+} uptake simply by adjusting contact time. The removal efficiency for K^+, Na^+ and Mn^{2+} is below 4%.

3.5 Comparison with other materials

Other MoS_2-based adsorbents reported in the literature have been compared with C-W-D-MoS_2 for their adsorption performance, particularly in terms of maximum adsorption capacity (q_m) and partition coefficients (K_d) (Table 3). Among these, C-W-D-MoS_2-0.03 exhibits outstanding performance for Hg(II), with a q_m of 1974.0 mg g^{-1}—superior to most reported materials. Although slightly lower than the 2563 mg g^{-1} reported by Kelong Ai *et al.*,[24] this difference can be attributed to the higher stacking degree of C-W-D-MoS_2-0.03 compared with W-DR-N-MoS_2 in the referenced study.[24] In C-W-D-MoS_2-0.03, agglomeration-induced overlapping partially hinders the interaction between S^{2-} and Hg^{2+} ions. Future research aimed at reducing MoS_2 agglomeration may further improve its adsorption efficiency.

In conclusion, C-W-D-MoS_2-0.03 demonstrates excellent adsorption performance and practical applicability, supported by its recyclability, straightforward preparation process, and scalability for large-scale production.

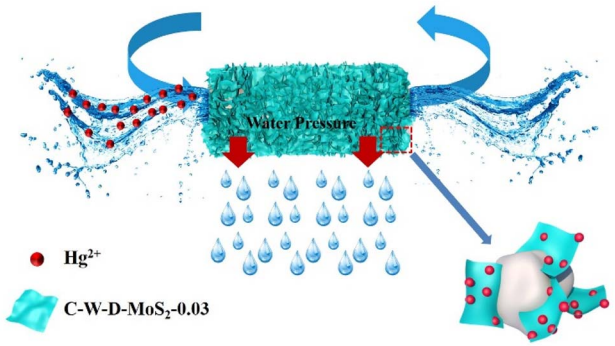

Fig. 12 Schematic illustrates the adsorption process of alumina inorganic membrane functionalized with C-W-D-MoS_2-0.03.

3.6 Laboratory application

To simulate practical applications in a laboratory setting, an alumina inorganic membrane functionalized with C-W-D-MoS_2-0.03 was fabricated and incorporated into a test device for Hg^{2+} adsorption. The corresponding photographs and SEM images of the functionalized membrane are shown in Fig. S8 and Fig. 10. As observed in Fig. S8, C-W-D-MoS_2-0.03 is uniformly distributed across both the inner and outer surfaces of the inorganic membrane. Moreover, Fig. 10 confirm that C-W-D-MoS_2-0.03 penetrates into the membrane pores. The loading capacity of C-W-D-MoS_2-0.03 per unit volume was determined to be 0.045 g cm^{-3}.

The schematic diagram of the laboratory test is shown in Fig. 11(a) and S9. A diaphragm pump was employed to continuously extract wastewater through the adsorption unit at a constant flow rate. The C-W-D-MoS_2-0.03-functionalized alumina membrane was installed at the adsorption site. To generate a pressure difference, hoses of two different diameters were incorporated into the circulation loop, with a 10 mm diameter hose connected to the adsorption chamber.

As shown in Fig. 11(b), after circulating 300 mL of Hg^{2+}-containing wastewater through the test device, the Hg(II) concentration in the filtrate was effectively reduced from 50 ppm to below 0.1 ppm, corresponding to a removal efficiency of more than 99.5% by the alumina inorganic membrane functionalized with C-W-D-MoS_2-0.03. As the treated wastewater volume increased, the system continued to perform efficiently, maintaining high adsorption efficiency even when the total volume reached 1 L. This device enables continuous wastewater treatment by simply replacing the used alumina inorganic membrane functionalized with C-W-D-MoS_2-0.03, thereby overcoming the challenges of recovering C-W-D-MoS_2-0.03 powder and avoiding the limitations of intermittent treatment. This approach demonstrates strong potential for continuous mercury-containing wastewater treatment in practical applications. Furthermore, Fig. 11(c) illustrates the recycling performance of the functionalized membrane; even after six adsorption cycles, the removal efficiency remained as high as 98%, confirming its excellent reusability.

Fig. 12 presents a schematic diagram of the adsorption process using the alumina inorganic membrane functionalized with C-W-D-MoS_2-0.03. As illustrated, wastewater infiltrates from the inner surface to the outer surface of the inorganic membrane due to the applied pressure difference. During this process, intimate contact occurs between the wastewater and the C-W-D-MoS_2-0.03 grown on the membrane, ensuring that Hg^{2+} ions are effectively adsorbed. Traditional powder-based adsorption processes are primarily governed by electrostatic and chemical interactions; however, in this testing device, water pressure additionally facilitates the adsorption of Hg^{2+} onto the C-W-D-MoS_2-0.03 surface. Consequently, the overall adsorption efficiency is significantly enhanced.

4 Conclusions

Carbon-modified C-W-D-MoS_2-x with expanded interlayer spacing and multiple exposed sulfur active sites was synthesized *via* a facile solvothermal method. The incorporation of carbon functional groups derived from citric acid hydrolysis synergistically enhanced the adsorption of Hg^{2+}. Among the prepared materials, C-W-D-MoS_2-0.03 exhibited outstanding adsorption performance for Hg^{2+}, with a K_d of 2.0×10^5 mL g^{-1}. The adsorption kinetics followed a pseudo-second-order model, while the isotherm data were best described by the Langmuir model, yielding a q_{max} of 1974.0 mg g^{-1}. For practical evaluation, an alumina inorganic membrane functionalized with C-W-D-MoS_2-0.03 was tested under dynamic conditions for Hg(II) removal from wastewater. The results showed that a removal efficiency of over 99% was maintained during continuous filtration of up to 1 L of Hg^{2+}-contaminated water. This approach effectively resolved the issues of adsorbent recovery and process interruption, making it feasible to achieve continuous treatment of mercury-containing wastewater in practical applications.

Author contributions

Mingmin Bai: conceptualization, methodology, writing – original draft, data curation. Wenyuan Guo: investigation, methodology. Yiyang Zhang: investigation, methodology, software. Ruiqiang Yang: writing – review. Weixin Li: software, validation, formal analysis, visualization, writing – review & editing.

Conflicts of interest

The authors have no competing interests to declare that are relevant to the content of this article.

Data availability

The data that support the findings of this study are available from the corresponding author upon reasonable request.

Supplementary information is available. See DOI: **https://doi.org/10.1039/d5ra04594k**.

Acknowledgements

This work was supported by the National Natural Science Foundation of China (Grant No. 52362003), National Natural Science Foundation of Jiangxi Province (Grant No. 20242BAB25320), Students innovation and entrepreneurship training program (Grant No. S202310408007) and Jingdezhen Science and Technology Plan Project(Grant No. 2023GY001-14, 20234ST003). Thank you to Engineer Han Qiang from the Analysis Center of Tsinghua University for his assistance in the testing process.

References

1 R. Sankaran, P. Loke Show, C.-W. Ooi, T. Chuan Ling, C. Shu-Jen, S.-Y. Chen and Yu-K. Chang, Feasibility assessment of removal of heavy metals and soluble microbial products from aqueous solutions using eggshell wastes, *Clean Technol. Environ*, 2020, **22**, 773–786, DOI: **10.1007/s10098-019-01792-z**.

2 Q. Zhou, N. Yang, Y. Li, B. Ren, X. Ding, H. Bian and X. Yao, Total concentrations and sources of heavy metal pollution in global river and lake water bodies from 1972 to 2017, *Glob. Ecol. Conserv.*, 2020, **22**, e00925, DOI: **10.1016/j.gecco.2020.e00925**.

3 W. S. Chai, J. Ying Cheun, P. Senthil Kumar, M. Mubashir, Z. Majeed, F. Banat, S.-H. Ho and P. L. Show, A review on conventional and novel materials towards heavy metal adsorption in wastewater treatment application, *J. Clean. Prod.*, 2021, **296**, 126589, DOI: **10.1016/j.jclepro.2021.126589**.

4 L. Liang, F. Xi, W. Tan, X. Meng, B. Hu and X. Wang, Review of organic and inorganic pollutants removal by biochar and biochar-based composites, *Biochar*, 2021, **3**, 255–281, DOI: **10.1007/s42773-021-00101-6**.

5 T. Kegl, A. Kosak, A. Lobnik, Z. Novak, A. K. Kralj and I. Ban, Adsorption of rare earth metals from wastewater by nanomaterials: A review, *J. Hazard. Mater.*, 2020, **386**, 121632, DOI: **10.1016/j.jhazmat.2019.121632**.

6 D. Tang, J. Li, Z. Yang, X. Jiang, L. Huang, X. Guo, Y. Li, J. Zh and X. Sun, Fabrication and mechanism exploration of oxygen-incorporated 1T-MoS_2 with high adsorption performance on methylene blue, *Chem. Eng. J.*, 2022, **428**, 130954, DOI: **10.1016/j.cej.2021.130954**.

7 T. Xu, W. Jie, P. He, J. Wu, N. Chen, E. Shi, C. Pan, X. Zhao and Y. Zhang, CuS-doped Ti_3C_2 MXene nanosheets for highly efficient adsorption of elemental mercury in flue gas, *Energy Fuel.*, 2022, **36**, 2503–2514, DOI: **10.1021/acs.energyfuels.1c03705**.

8 F. Liu, W. Xiong, X. Feng, L. Shi, D. Chen and Y. Zhang, A novel monolith ZnS-ZIF-8 adsorption material for ultraeffective Hg (II) capture from wastewater, *J. Hazard. Mater.*, 2019, **367**, 381–389, DOI: **10.1016/j.jhazmat.2018.12.098**.

9 G. M. Neelgund, E. A. Jimenez, R. L. Ray and M. D. Kurkuri, Facilitated adsorption of mercury(II) and chromium(VI) ions over functionalized carbon nanotubes, *Toxics*, 2023, **11**, 545, DOI: **10.3390/toxics11060545**.

10 H. Chen, M. Wang, L. Wang, M. Zhou, H. Wu and H. Yang, Enhanced separation performance of Hg^{2+} in desulfurization wastewater using a tannin acid reduced graphene oxide membrane, *Sep. Purif. Technol.*, 2021, **274**, 119017, DOI: **10.1016/j.seppur.2021.119017**.

11 G. Chen, H. Zhao, X. Li and S. Xia, Theoretical investigation of the chloride effect on aqueous Hg(II) adsorption on the kaolinite(001) surface, *Appl. Clay Sci.*, 2021, **210**, 106120, DOI: **10.1016/j.clay.2021.106120**.

12 R. Shahrokhi-Shahraki, C. Benally, M. G. El-Din and J. Park, High efficiency removal of heavy metals using tire-derived activated carbon *vs.* commercial activated carbon: Insights into the adsorption mechanisms, *Chemosphere*, 2021, **264**, 128455, DOI: **10.1016/j.chemosphere.2020.128455**.

13 B. Zen, W. Wang, S. He, G. Lin, D. Wenjia, J. Chang and Z. Ding, Facile synthesis of zinc-based organic framework for aqueous Hg (II) removal: Adsorption performance and mechanism, *Nano Mater. Sci*, 2021, **3**, 429–439, DOI: **10.1016/j.nanoms.2021.06.005**.

14 M. Harja and G. Ciobanu, Studies on adsorption of oxytetracycline from aqueous solutions onto hydroxyapatite, *Sci.Total.Environ.*, 2018, **628–629**, 36–43, DOI: **10.1016/j.scitotenv.2018.02.027**.

15 A. E. Burakov, E. V. Galunin, I. V. Burakova, A. E. Kucherova, S. Agarwal, A. G. Tkachev and V. K. Gupta, Adsorption of heavy metals on conventional and nanostructured materials for wastewater treatment purposes: A review, *Ecotoxicol. Environ. Saf.*, 2018, **148**, 702–712, DOI: **10.1016/j.ecoenv.2017.11.034**.

16 S. Saadi Fiyadh, M. A. AlSaadi, Z. J. Wan, K. AlO. Mohamed, S. Saadi Fayae, S. M. Nuruol, S. H. Lai and A. El-Shafie, Review on heavy metal adsorption processes by carbon nanotubes, *J. Cleaner Prod.*, 2019, **230**, 783–793, DOI: **10.1016/j.jclepro.2019.05.154**.

17 O. Amiri, H. Emadi, S. Seyed Mostafa Hosseinpour-Mashkani, M. Sabet and M. Mohammadi Rad, Simple and surfactant free synthesis and characterization of CdS/ZnS core–shell nanoparticles and their application in the removal of heavy metals from aqueous solution, *RSC Adv.*, 2014, **4**, 10990–10996, DOI: **10.1039/c3ra46267f**.

18 H. Li, S. Feng, Z. Yang, J. Yang, S. Liu, Y. Hu, L. Zhong and W. Qu, Density functional theory study of mercury adsorption on CuS surface: Effect of typical flue gas components, *Energy Fuels*, 2019, **33**, 1540–1546, DOI: **10.1021/acs.energyfuels.8b03585**.

19 S. Li, X. Chen, L. Mingjie, X. Cheng, Y. Lon, W. Li, Z. Ca, X. Ton, W. Huan and D. Liu, Hollow Co_3S_4 polyhedron decorated with interlayer-expanded MoS_2 nanosheets for effcient tetracycline removal from aqueous solution, *Chem. Eng. J.*, 2022, **441**, 136006, DOI: **10.1016/j.cej.2022.136006**.

20 W. Zhan, F. Jia, Y. Yuan, C. Liu, K. Sun, B. Yang and S. Song, Controllable incorporation of oxygen in MoS_2 for efficient adsorption of Hg^{2+} in aqueous solutions, *J. Hazard. Mater.*, 2022, **384**, 121382, DOI: **10.1016/j.jhazmat.2019.121382**.

21 Y. Wang, H. Xu, X. Zhao, H. Meng, Y. Lu and C. Li, Alkynyl functionalized MoS_2 mesoporous materials with superb

adsorptivity for heavy metal ions, *J. Hazard. Mater.*, 2022, **424**, 127579, DOI: 10.1016/j.jhazmat.2021.127579.

22 C. Liu, F. Jia, Q. Wang, B. Yan and S. Song, Two-dimensional molybdenum disulfide as adsorbent for high-efficient Pb(II) removal from water, *Appl. Mater. Today*, 2017, **9**, 220–228, DOI: 10.1016/j.apmt.2017.07.009.

23 N. Kumar, E. Fosso-Kankeu and S. S. Ray, Achieving controllable MoS_2 nanostructures with increased interlayer spacing for efficient removal of Pb(II) from aquatic systems, *ACS Appl. Mater. Interfaces*, 2019, **11**, 19141–19155, DOI: 10.1021/acsami.9b03853.

24 K. Ai, C. Ruan, M. She and L. Lu, MoS_2 nanosheets with widened interlayer spacing for high-efficiency removal of mercury in aquatic systems, *Adv. Funct. Mater.*, 2016, **26**, 5542–5549, DOI: 10.1002/adfm.201601338.

25 Y. Song, M. Lu, B. Huang, D. Wang, G. Wang and L. Zhou, Decoration of defective MoS_2 nanosheets with Fe_3O_4 nanoparticles as superior magnetic adsorbent for highly selective and efficient mercury ions (Hg^{2+}) removal, *J. Alloys Compd.*, 2018, **737**, 113–121, DOI: 10.1016/j.jallcom.2017.12.087.

26 W. Jie, P. He, J. Wu, N. Chen, T. Xu, E. Shi, C. Pan, X. Zhao and Y. Zhang, Conversion of 2H MoS_2 to 1 T MoS_2 via lithium ion doping: Effective removal of elemental mercury, *Chem. Eng. J.*, 2022, **428**, 131014, DOI: 10.1016/j.cej.2021.131014.

27 Y. Dua, H. Fu, L. Zhang, R. Ga, S. Qi, Z. Chen and H. Du, Embedding of ultra-dispersed MoS_2 nanosheets in N,O heteroatom-modified carbon nanofibers for improved adsorption of Hg^{2+}, *Compos. Commun.*, 2022, **31**, 101106, DOI: 10.1016/j.coco.2022.101106.

28 S. Yang, Y. Chen, T. E, Y. Wan, L. Liu, Y. L, D. Wan and J. Qian, Construction Si-O-Mo bond via etching method: enhancing selective adsorption capacity of MoS_2/montmorillonite to Pb^{2+}, *Mater. Today Chem.*, 2022, **26**, 101056, DOI: 10.1016/j.mtchem.2022.101056.

29 Y. Xiao, Q. Li, Y. Huang, F. Tia, T. Jia, M. Zhang, Q. Liu, J. Wu, Y. Peng and X. Wang, Coordinative sulfur site over flower-structured MoS_2 for effcient elemental mercury uptake from coal-fired flue gas, *Chem. Eng. J.*, 2022, **434**, 134649, DOI: 10.1016/j.cej.2022.134649.

30 S. Sang, S. Yang, A. Guo, X. Gao, Y. Wang, C. Zhang, F. Cui and X. Yang, Hydrothermal synthesis of carbon nano-onions from citric acid, *Chem. Asian J.*, 2020, **15**, 3428–3431, DOI: 10.1002/asia.202000983.

31 M. Bai, W. Li, H. Yang, W. Dong, Q. Wang and Q. Chang, Morphology-controlled synthesis of MoS_2 using citric acid as a complexing agent and self-assembly inducer for high electrochemical performance, *RSC Adv.*, 2022, **12**, 28463, DOI: 10.1039/d2ra05351a.

32 D. Wang, X. Zhang, S. Bao, Z. Zhang, H. Fei and Z. Wu, Phase-engineering of multiphasic 1T/2H MoS_2 catalyst for highly efficient hydrogen evolution, *J. Mater. Chem. A*, 2017, **5**, 2681–2689, DOI: 10.1039/c6ta09409k.

33 Li-Na Wang, Xu Wu, Fu-T. Wang, X. Chen, J. Xu and Ke-J. Huang, 1T-Phase MoS_2 with large layer spacing supported on carbon cloth for high-performance Na^+ storage, *J. Colloid Interface Sci.*, 2021, **583**, 579–585, DOI: 10.1016/j.jcis.2020.09.055.

34 H. Zha, S. Cui, G. Li, N. Li and X. Li, 1T- and 2H-mixed phase MoS_2 nanosheets coated on hollow mesoporous TiO_2 nanospheres with enhanced photocatalytic activity, *J. Colloid Interface Sci.*, 2020, **567**, 10–17, DOI: 10.1016/j.jcis.2020.01.100.

35 X. Che, Z. Wan, Y. Wei, X. Zhang, Q. Zhang, L. Gu, L. Zhang, N. Yang and R. Yu, High phase-purity 1T-MoS_2 ultrathin nanosheets by a spatially confined template, *Angew. Chem., Int. Ed.*, 2019, **131**, 1–5, DOI: 10.1021/acssuschemeng.9b02383.

36 Q. Liu, F. Qi, W. Chu, Y. Wan, X. Li, W. Xu, M. Habib, T. Shi, Yu Z. D. Liu, T. Xiang, A. Khalil, X. Wu, M. Chhowalla, P. M. Ajayan and Li Song, Electron-doped 1T-MoS2 via interface engineering for enhanced electrocatalytic hydrogen evolution, *Chem. Mater*, 2017, 4738–4744, DOI: 10.1021/acs.chemmater.7b00446.

37 D. Wang, B. Su, Y. Jiang, L. Lu, K. Boon, W. Zhuangzhi and L. Fangyang, Polytype 1T/2H MoS2 heterostructures for efficient photoelectrocatalytic hydrogen evolution, *Chem. Eng. J.*, 2017, **330**, 102–108, DOI: 10.1016/j.cej.2017.07.126.

38 L. Zhi, W. Zuo, F. Chen and B. Wang, 3D MoS_2 composition aerogels as chemosensors and adsorbents for colorimetric detection and high-capacity adsorption of Hg^{2+}, *ACS Sustain. Chem. Eng.*, 2016, **4**, 3398–3408, DOI: 10.1021/acssuschemeng.6b00409.

39 J. Kibsgaard, Z. Chen, B. N. Reinecke and T. F. Jaramillo, Engineering the surface structure of MoS_2 to preferentially expose active edge sites for electrocatalysis, *Nat. Mater.*, 2012, **11**, 963–969, DOI: 10.1038/NMAT3439.

40 X. Fan, P. Xu, D. Zhou, Y. Sun, Y. C. Li, M. An T. Nguyen, M. Terrones and T. E. Mallouk, Fast and efficient preparation of exfoliated 2H MoS_2 nanosheets by sonication-assisted lithium intercalation and infrared laser-induced 1T to 2H phase reversion, *Nano Lett.*, 2015, **15**, 5956–5960, DOI: 10.1021/acs.nanolett.5b02091.

41 F. Ma, Y. Liang, P. Zhou, F. Tong, Z. Wang, W. Peng, Y. Liu, Y. Dai, Z. Zheng and B. Huang, One-step synthesis of Co-doped 1T-MoS_2 nanosheets with efficient and stable HER activity in alkaline solutions, *Mate. Chem. Phys.*, 2020, **244**, 122642, DOI: 10.1016/j.matchemphys.2020.122642.

42 H. Guo, L. Wang, W. You, L. Yang, X. Li, G. Chen, Z. Wu, X. Qian, M. Wang and R. Che, Engineering phase transformation of MoS_2/RGO by N-doping as an excellent microwave absorber, *ACS Appl. Mater. Interfaces.*, 2020, **12**, 16831–16840, DOI: 10.1021/acsami.0c01998.

43 T. Wang, C. Su, M. Yang, G. Zhao, S. Wang, F. Ma, L. Zhang, Y. Shao, Y. Wu, B. Huang and H. Xiaopeng, Phase-transformation engineering in MoS_2 on carbon cloth as flexible binder-free anode for enhancing lithium storage, *J. Alloys. Compd.*, 2017, **716**, 112–118, DOI: 10.1016/j.jallcom.2017.05.071.

44 I. Abouda, S. Walha, S. Bouattour, A. M. Botelho do Reg, A. M. Ferraria, A. S. C. Sousa, N. Cost and S. Boufi, Cotton fabric functionalized with nanostructured MoS_2: Efficient adsorbent for removal of Pb, Hg, Cd and Cr from water, *J.*

Environ. Chem. Eng., 2022, **10**, 108583, DOI: 10.1016/j.jece.2022.108583.

45 T. Hua, H. Junhui and M. Hu, A selectivity-controlled adsorbent of molybdenum disulfide nanosheets armed with superparamagnetism for rapid capture of mercury ions, *J. Colloid Interface Sci.*, 2019, **551**, 251–260, DOI: 10.1016/j.jcis.2019.05.027.

46 X. Hu, C. Chen, D. Zhang and Y. Xue, Kinetics, isotherm and chemical speciation analysis of Hg(II) adsorption over oxygen-containing MXene adsorbent, *Chemosphere*, 2021, **278**, 130206, DOI: 10.1016/j.chemosphere.2021.130206.

47 F. Jia, Q. Wang, J. Wu, Y. Li and S. Song, Two-dimensional molybdenum disulfide as a superb adsorbent for removing Hg^{2+} from water, Sustainable, *Chem. Eng.*, 2017, **5**, 7410–7419, DOI: 10.1021/acssuschemeng.7b01880.

48 L. A. Chang, Z. A. Shilin, Y. B. Bingqiao, F. Jia and S. Song, Simultaneous removal of Hg^{2+}, Pb^{2+} and Cd^{2+} from aqueous solutions on multifunctional MoS_2, *J. Mol. Liq.*, 2019, **296**, 111987, DOI: 10.1016/j.molliq.2019.111987.

49 L. Zhi, W. Zuo, F. Chen and B. Wang, 3D MoS_2 Composition aerogel as chemosensors and adsorbents for colorimetric detection and high-capacity adsorption of Hg^{2+}, Sustainable, *Chem. Eng.*, 2016, **4**, 3398–3408, DOI: 10.1021/acssuschemeng.6b00409.

50 M. M. Hyland, G. E. Jean and G. M. Bancrof, XPS and AES studies of Hg(II) sorption and desorption reactions on sulphide minerals, *Geochim. Cosmochim. Ac.*, 1990, **54**, 1957–1967, DOI: 10.1016/0016-7037(90)90264-L.

51 Yu-T. Zhuang, X. Zhang, D.-H. Wang, Y.-L. Yu and J.-H. Wang, Three-dimensional molybdenum disulfide/graphene hydrogel with tunable heterointerfaces for high selective Hg(II) scavenging, *J. Colloid Interface Sci.*, 2018, **514**, 715–722, DOI: 10.1016/j.jcis.2017.12.082.

52 W. Jie, P. He, J. Wu, N. Chen, T. Xu, E. Shi, C. Pan, X. Zhao and Y. Zhang, Conversion of 2H MoS_2 to 1 T MoS_2 via lithium ion doping: Effective removal of elemental mercury, *Chem. Eng. J.*, 2022, **428**, 131014, DOI: 10.1016/j.cej.2021.131014.

53 R. Ma, D. Nie, M. Sang, W. Wang and G. Nie, Adsorption of Rhodamine B and Pb(II) from aqueous solution by MoS_2 nanosheet modifed biochar: Fabrication, performance, and mechanisms, *Bioresource. Technolo.*, 2023, **386**, 129548, DOI: 10.1016/j.biortech.2023.129548.